Model-Free and Analytical EAP Reconstruction via Spherical Polar Fourier Diffusion MRI

Jian Cheng[1,2], Aurobrata Ghosh[1], Tianzi Jiang[2], and Rachid Deriche[1]

[1] Athena Project Team, INRIA Sophia Antipolis – Méditerranée, France
[2] Center for Computational Medicine, LIAMA, Institute of Automation,
Chinese Academy of Sciences, China
Jian.Cheng@sophia.inria.fr

Abstract. How to estimate the diffusion Ensemble Average Propagator (EAP) from the DWI signals in **q**-space is an open problem in diffusion MRI field. Many methods were proposed to estimate the Orientation Distribution Function (ODF) that is used to describe the fiber direction. However, ODF is just one of the features of the EAP. Compared with ODF, EAP has the full information about the diffusion process which reflects the complex tissue micro-structure. Diffusion Orientation Transform (DOT) and Diffusion Spectrum Imaging (DSI) are two important methods to estimate the EAP from the signal. However, DOT is based on mono-exponential assumption and DSI needs a lot of samplings and very large b values. In this paper, we propose Spherical Polar Fourier Imaging (SPFI), a novel model-free fast robust analytical EAP reconstruction method, which almost does not need any assumption of data and does not need too many samplings. SPFI naturally combines the DWI signals with different b-values. It is an analytical linear transformation from the **q**-space signal to the EAP profile represented by Spherical Harmonics (SH). We validated the proposed methods in synthetic data, phantom data and real data. It works well in all experiments, especially for the data with low SNR, low anisotropy, and non-exponential decay.

1 Introduction

Diffusion MRI is a non-invasive technique to explore the complex white matter by probing the diffusion process of water molecules. EAP has the full information about the diffusion process. Estimating the EAP is at the heart of dMRI. When the narrow pulse condition is met, EAP is related with the signal attenuation by a Fourier transform.

$$P(\mathbf{R}) = \int E(\mathbf{q})e^{-2\pi i \mathbf{q} \cdot \mathbf{R}} d\mathbf{q}, \tag{1}$$

where **R** is the displacement vector in **R**-space, and **q** is the reciprocal vector in **q**-space. There are many articles about Orientation Distribution Function (ODF) in High Angular Resolution Diffusion Imaging (HARDI) [1,2]. But ODF is just one of the features of EAP and it has no radial information.

Historically, DTI was proposed by assuming $P(\mathbf{R})$ as a Gaussian distribution [3]. It is actually a model-based method to estimate $P(\mathbf{R})$, which cannot describe the non-Gaussian diffusion. Diffusion Spectrum Imaging (DSI) [4] is a well known model-free

method to estimate EAP. The main shortcoming of DSI is that it uses a numerical Fourier Transform and needs very large range of b values and a lot of samplings.

Diffusion Orientation Transform (DOT) [6] is a fast analytical method based on mono-exponential decay assumption on $E(\mathbf{q})$. It was proposed to relax the Gaussian assumption in DTI to the assumption of mono-exponential decay. This assumption lets us have the full information about $E(\mathbf{q})$ in the whole 3D $\mathbf{q}$-space from the $E(q_0\mathbf{u})$ only in a single shell. Then EAP profile at a given radius R_0 could be calculated analytically. However the estimated EAP is the true PDF convolved by the Fourier transform of the function $E(q,\mathbf{u})^{q^2/q_0^2}E(q,\mathbf{u})^{-1}$ [6], where $\mathbf{q} = q\mathbf{u}$, $q = \|\mathbf{q}\|$. It was shown surprisingly that the estimated $\tilde{P}(R\mathbf{r})$ in some synthetic experiments is sharper than the real $P(R\mathbf{r})$. But since this effect comes from the intrinsic modeling error, it is still not clear whether DOT can work well in the complex real data with non-exponential decay, low anisotropy and low SNR. The author in [6] has extended mono-exponential model to multi-exponential model so that it can reduce the modeling error and work for the data from multiple shells. However, it is impractical because a nonlinear fitting is needed for every direction [6], suffering from limited samples, local minima, computational complexity, and an analytic solution exists only when three b values satisfy an arithmetic process. Diffusion Propagator Imaging (DPI) [7] is another analytical estimation which assumes the $E(\mathbf{q})$ can be represented as the form of the solution of 3D Laplacian equation. It seems to work well just with small number of samplings. However, that assumption is unrealistic for $E(\mathbf{q})$, since $E(0)$ does not exist based on that assumption.

$$E(\mathbf{q}) = \sum_{n=0}^{N}\sum_{l=0}^{L}\sum_{m=-l}^{l} a_{n,l,m}R_n(\|\mathbf{q}\|)Y_l^m(\mathbf{u}) \qquad B_{n,l,m}(\mathbf{q}) = R_n(\|\mathbf{q}\|)Y_l^m(\mathbf{u}) \qquad (2)$$

$$R_n(\|\mathbf{q}\|) = \kappa_n(\zeta)\exp\left(-\frac{\|\mathbf{q}\|^2}{2\zeta}\right)L_n^{1/2}(\frac{\|\mathbf{q}\|^2}{\zeta}) \qquad \kappa_n(\zeta) = \left[\frac{2}{\zeta^{3/2}}\frac{n!}{\Gamma(n+3/2)}\right]^{1/2} \qquad (3)$$

Compared with Laplacian equation modeling in [7], Spherical Polar Fourier Expression (SPFE) of $E(\mathbf{q})$ seems better. It was proposed to sparsely represent $E(\mathbf{q})$ [8]. See formulae (2),(3), where $Y_l^m(\mathbf{u})$ is the l order m degree Spherical Harmonic (SH) basis and $R_n(q)$ is the Gaussian-Laguerre polynomial basis. Since $B_{n,l,m}(\mathbf{q})$ is the orthonormal basis in R^3, any $E(\mathbf{q})$ could be represented by a linear combination of $\{B_{n,l,m}\}$. While Laplacian equation modeling can not. In [8], the authors proposed two methods to estimate the coefficients $\{a_{n,l,m}\}$, a least square fit and a nonlinear robust estimation which considers the Rician noise. After $\{a_{n,l,m}\}$ are estimated, a inner product of $a_{l,n,m}$ and a kernel $b_{n,l,m}$ was used to calculate some features of $P(\mathbf{R})$, e.g. the ODF in [1], EAP profile [8]. The problem of [8] is that the kernel $b_{n,l,m}$ needs to be calculated numerically from FFT for every direction or calculated for one direction then rotated by Wigner rotation matrix for other directions. For EAP profile it can bring some numerical error since the kernel has some delta functions inside.

In this paper, based on the SPFE in [8], we propose Spherical Polar Fourier Imaging (SPFI), a novel technique for model-free analytical reconstruction of the EAP profile from the signals in different Q-shells. It is a linear transformation from the coefficients $\{a_{n,l,m}\}$ of the signal $E(\mathbf{q})$ to the coefficients $\{c_{l,m}\}$ of EAP profile $P(R_0)$ represented by SH for a given R_0. First we deduce the transform for EAP profile. Then, we perform the

method in some non-exponential synthetic data, a challenging phantom data and a real monkey data with several b values.

2   Analytical EAP Profile Estimation Based on SPF

Our method is close in spirit to the methods in DOT [6] and DPI [7]. Adding a strong assumption (in DOT) or choosing a good representation of $E(\mathbf{q})$ (in DPI and SPFI) will dramatically simplify the Fourier transform in (1).

2.1   Estimation of EAP Profile

SPFE is a kind of orthonormal basis representation and it was shown in [8] that it can sparsely represent the diffusion signal. See formula (2). After we estimate the coefficients of the signal via the methods in [8], we proved that there is a linear, analytical solution to get the coefficients of the EAP profile at a given radius R_0 under SH representation. Firstly consider the plane wave equation in spherical coordinates in (4)

$$e^{\pm 2\pi i \mathbf{q} \cdot \mathbf{R}} = 4\pi \sum_{l=0}^{\infty} \sum_{m=-l}^{l} (\pm i)^l j_l(2\pi qR) Y_l^m(\mathbf{u}) Y_l^m(\mathbf{r}), \tag{4}$$

where $j_l(x)$ is the l-th order spherical Bessel function. $j_l(x) = \sqrt{\frac{\pi}{2x}} J_{l+0.5}(x)$, $J_{l+0.5}(x)$ is the Bessel function of the first kind. Then put the formula (2) into formula (1).

$$P(R_0\mathbf{r}) = 4\pi \int \left\{ \sum_{n=0}^{N} \sum_{l=0}^{L} \sum_{m=-l}^{l} a_{n,l,m} R_n(q) Y_l^m(\mathbf{u}) \right\} \left\{ \sum_{l'=0}^{\infty} \sum_{m'=-l'}^{l'} (-i)^{l'} j_{l'}(2\pi qR_0) Y_{l'}^{m'}(\mathbf{u}) Y_{l'}^{m'}(\mathbf{r}) \right\} d\mathbf{q}$$

$$= 4\pi \sum_{l=0}^{L} \sum_{m=-l}^{l} (-1)^{l/2} \sum_{n=0}^{N} \left\{ \underbrace{\int_0^{\infty} j_l(2\pi qR_0) R_n(q) q^2 dq}_{I_{l,n}(R_0)} \right\} a_{n,l,m} Y_l^m(\mathbf{r}) \tag{5}$$

where we use the orthonormal property of SHs, i.e. $\int_{S^2} Y_l^m(\mathbf{u}) Y_{l'}^{m'}(\mathbf{u}) d\mathbf{u} = \delta_{ll'} \delta_{mm'}$, and define $I_{l,n}(R_0) = \int_0^{\infty} j_l(2\pi qR_0) R_n(q) q^2 dq$. It should be noted that in formula (2), if we fix the SH as the spherical basis and use another radial basis $R_n'(q)$, the equation (5) also holds. We choose Gaussian-Laguerre radial basis because it could sparsely represent $E(\mathbf{q})$ [8]. Considering in (3) $L_n^{1/2}(x) = \sum_{i=0}^n l_n^i x^i$, $l_n^i = (-1)^i \binom{n+0.5}{n-i} \frac{1}{i!}$, we have

$$I_{l,n}(R_0) = \frac{\kappa_n(\zeta)\zeta^{1.25}}{2\sqrt{R_0}} \sum_{i=0}^{n} l_n^i \int_0^{\infty} x^{2i+1.5} J_{l+0.5}(2\pi R_0 \sqrt{\zeta} x) \exp(-0.5x^2) dx \tag{6}$$

Based on the property of Bessel function [9], we have

$$\int_0^{\infty} x^{\mu} \exp(-\alpha x^2) J_{\nu}(\beta x) dx = \frac{\beta^{\nu} \Gamma(0.5\nu + 0.5\mu + 0.5)}{2^{\nu+1} \alpha^{0.5(\mu+\nu+1)} \Gamma(\nu + 1)} 1F1(\frac{\mu + \nu + 1}{2}; \nu + 1; -\frac{\beta^2}{4\alpha}) \tag{7}$$

where $1F1$ is the confluent hypergeometric function of the first kind. $1F1(a; b; x) = \sum_{k=0}^{\infty} \frac{(a)_k x^k}{(b)_k k!}$, $(a)_k = (a(a+1)...(a+l-1))$, with $(a)_0 = 1$. Here in (6) $\alpha = 0.5, \beta = 2\pi R_0 \sqrt{\zeta}$, $\nu = l + 0.5, \mu = 2i + 1.5$, then we get

$$I_{l,n}(R_0) = \frac{\kappa_n(\zeta)\zeta^{0.5l+1.5}\pi^{l+0.5}R_0^l}{\Gamma(l+1.5)} \sum_{i=0}^{n} l_n^i 2^{0.5l+i-0.5} \Gamma(0.5l+i+1.5) 1F1(\frac{2i+l+3}{2}; l+\frac{3}{2}; -2\pi^2 R_0^2\zeta)$$

Put it into (5), we have

$$P(R_0\mathbf{r}) = \sum_{l=0}^{L} \sum_{m=-l}^{l} \left\{ 4(-1)^{l/2} \frac{\zeta^{0.5l+1.5}\pi^{l+1.5}R_0^l}{\Gamma(l+1.5)} \sum_{n=0}^{N} f_{n,l,m}(\zeta, R_0) a_{n,l,m} \right\} Y_l^m(\mathbf{u}) \qquad (8)$$

$$\boxed{c_{l,m} = 4(-1)^{l/2} \frac{\zeta^{0.5l+1.5}\pi^{l+1.5}R_0^l}{\Gamma(l+1.5)} \sum_{n=0}^{N} f_{n,l,m}(\zeta, R_0) a_{n,l,m}} \qquad (9)$$

$$\boxed{f_{n,l,m}(\zeta, R_0) = \kappa_n(\zeta) \sum_{i=0}^{n} (-1)^i \binom{n+0.5}{n-i} \frac{1}{i!} 2^{0.5l+i-0.5} \Gamma(0.5l+i+1.5) 1F1(\frac{2i+l+3}{2}; l+\frac{3}{2}; -2\pi^2 R_0^2\zeta)}$$
$$(10)$$

Now we get the linear transform from $\{a_{n,l,m}\}$ to $\{c_{l,m}\}$, which could be implemented as an matrix multiplication. Moreover please note the important difference between SPFI and DOT. Here our transformation is independent with the data, since $f_{n,l,m}(\zeta, R_0)$ is just dependent on ζ and R_0. Once we give a R_0 and the basis, we have the transform. While in DOT, the transform is dependent on the ADC, which could brings some numerical errors. See appendix A in [6] for error analysis. Similarly with the appendix in [6], here the confluent hypergeometric function $1F1$ could also be calculated from an analytical solution. Actually in practice a numerical truncated approximation of $1F1$ is also acceptable, since in SPFI we just need the values of $1F1$ only at the fixed value $-2\pi^2 R_0^2\zeta$ and the transform matrix just needs to be calculated only once. Another important similarity with DOT is that if we just choose $N = 0$ in radial part, our transform will be the DOT, which could be seen from the formulae (9), (10). That is true since the order 0 of the radial basis follows mono-exponential decay. However, in SPFI we should use $N \geq 1$ to describe anisotropic decay, since the order 0 in (2) is just an isotropic part.

2.2 Zero Displacement Probability

The $Po = P(0)$ is the probability of water molecules that minimally diffuse within the diffusion time $\triangle$ [5]. The Po map could be used in tissue segmentation and some other applications [5]. In SFPI, we can easily estimate Po from (2), or by setting $R_0 = 0$ in (6), (5). These two ways are equivalent. Since $\int_0^\infty \exp(-st)t^\alpha L_n^\alpha(t)dt = \frac{\Gamma(\alpha+n+1)(s-1)^n}{n!s^{\alpha+n+1}}$ [9] and $\int_{S^2} Y_l^m(\mathbf{u})d\mathbf{u} = \sqrt{4\pi}\delta_{l0}\delta_{m0}$ we have

$$Po = \iiint E(\mathbf{q})d\mathbf{q} = \sum_{n=0}^{N} \sum_{l=0}^{L} \sum_{m=-l}^{l} a_{n,l,m} \left\{ \int_0^\infty R_n(q)q^2 \right\} \left\{ \int_{S^2} Y_l^m(\mathbf{u})d\mathbf{u} \right\} \qquad (11)$$

$$= \sqrt{8\pi} \sum_{n=0}^{N} (-1)^n \kappa_n(\zeta)\zeta^{1.5} \frac{\Gamma(n+1.5)}{n!} a_{n,0,0} \qquad (12)$$

$$= \boxed{4\sqrt{\pi}\zeta^{\frac{3}{4}} \sum_{n=0}^{N} (-1)^n \sqrt{\frac{\Gamma(n+1.5)}{n!}} a_{n,0,0}} \qquad (13)$$

2.3   Implementation of Methods

The Implementation includes two steps. The first step is to estimate coefficients $\{a_{n,l,m}\}$ from the signals $\{E(\mathbf{q}_i)\}$. The second step is the linear analytical transform proposed above from $\{a_{n,l,m}\}$ to $\{c_{l,m}\}$, which is actually independent of the first step. The whole estimation error is just from the first step, since the second step is analytical and compact. [8] suggested two methods to estimate $\{a_{n,l,m}\}$, a linear least square (LS) fitting with regularization in the radial and spherical parts, and a non-linear PDE based optimization process, which considers the Rician noise. Here we choose the LS method, known to be faster, in the first step. We suggest that the Rician correction could be performed directly on the DWI data as a pre-processing step [10,11], although in our experiments to perform an appropriate comparison of methods we did not perform any Rician correction.

For LS estimation, denote signal vector by $E = [E(\mathbf{q}_i)]_{S \times 1}$, the basis matrix by $M = [R_n(\mathbf{q})Y_l^m(\mathbf{u})]_{S \times 0.5(L+1)(L+2)(N+1)}$, and the spherical and radial regularization diagonal matrices respectively by $L = [l(l+1)]$ and $N = [n(n+1)]$. Then the coefficient vector $A = (M^T M + \lambda_l L^T L + \lambda_n N^T N)M^T E$, where λ_l and λ_n are the regularization terms for spherical and radial parts. For the second step, the linear transformation in (9), (10) could be also implemented as a matrix multiplication, i.e. $C = FA$. Thus we can combine this two steps or perform separately. To combine two steps, $C = \{F(M^T M + \lambda_l L^T L + \lambda_n N^T N)M^T\}E$. The matrix of the whole process, $F(M^T M + \lambda_l L^T L + \lambda_n N^T N)M^T$, is independent with E and needs to be calculated only once for the whole data set. It makes our method extremely fast. Another option is to separate these two steps. and store $a_{n,l,m}$ once it is estimated in the first step. Then estimating the coefficients for EAP profile at a given R_0 could be performed directly on the stored $\{a_{n,l,m}\}$. That means we just need to calculate $\{a_{n,l,m}\}$ once and could re-calculate different EAP profiles in different radii very fast. The main computation complex is in the estimation of $a_{n,l,m}$. But it is still very fast if least square fitting is used.

There are two important points to consider in the implementation. The first one is about $E(0)$. If a data set has several b values, $b_1, b_2..., b_N$, we actually use $N + 1$ b values, considering $b_0 = 0$ and $E(0) = 1$ for any $\mathbf{u} \in S^2$, which makes our estimation more reasonable and accurate. Otherwise, there is no warranty for the estimated signal $\tilde{E}(0) = 1$. Another advantage is that for the single shell HARDI data, considering $b = 0$ can let us have 2 shells, which will largely improve the results. The second one is how to determine the parameter ζ in basis. The authors in [8] proposed an experience strategy for it, which is dependent on the radial truncation order N. However, we think the parameter should be just dependent on the signal, not on the basis order. Considering $E(\mathbf{q}) = \exp(-4\pi^2\tau q^2 D)$, $b = 4\pi^2\tau q^2$, and a typical diffusion coefficient of $D = 0.7 \times 10^{-3} mm^2/s$, a typical b-value $b = 3000s/mm^2$, we set $\zeta = \frac{1}{8\pi^2\tau \times 0.7 \times 10^{-3}}$. If $4\pi^2\tau = 1$, then ζ is about 700. In our experiments we always set $\zeta = 700$.

3   Results on Synthetic, Phantom and Real Data

Synthetic data. Gaussian mixture model $S(\mathbf{q}_s) = \sum_{i=1}^{M} p_i G_i(\mathbf{q}_s)$, $G_i(\mathbf{q}_s) = \exp(-q_s^2 \mathbf{u}_s^T \mathbf{D}_i \mathbf{u}_s)$ has been used widely to generate synthetic data [2,13]. However, it could bias the results in favor of those methods assuming a model based on Gaussian

Table 1. For each configuration in each column, the left part and the right part show, respectively for Gaussian mixture model and non-Gaussian mixture model, the percentage of correct number of detected maximum of the estimated EAP profile and the mean of angular error. The first four rows recorded the performance of DOT on single shell data [6] with 81 gradient directions on the hemisphere. The last row is the results of our methods using 4 shells.

b value	(1, [1.1,0.5,0.5]e-3, 10, —)	(2, [1.3,0.4,0.4]e-3, 10, 90)	(2, [1.7,0.3,0.3]e-3, 35, 60)	(2,[1.7,0.3,0.3]e-3, 20, 65)
500	(28.0%,13.5°)(55.7%,12.6°)	(35.0%,27.3°)(49.9%,25.4°)	(0.4%,26.8°)(0.3%,26.8°)	(3.4%,28.5°)(3.6%,29.4°)
1000	(82.1%,8.9°)(72.5%,10.7°)	(61.4%,18.9°)(57.4%,20.6°)	(0.4%,26.8°)(1.8%,26.8°)	(9.2%,28.8)(6.9%,28.2°)
2000	(80.1%,8.3°)(49.0%,11.1°)	(67.5%,13.0°)(56.7%,18.4°)	(20.7%,26.14°)(15.8%,25.7°)	(46.7%,9.4°)(36.2%,11.2°)
3000	(23.1%,10.9°)(9.5%,13.4°)	(44.6%,16.1°)(32.7%,21.5°)	(58.9%,7.8°)(47.3%,7.8°)	(87.5%,5.0°)(76.1%,6.4°)
4 shells	(99.3%,6.7°)(89%,8.9°)	(96.1%,9.1°)(83.5%,12.3°)	(81.8%,4.8°)(62.1%,6.5°)	(95.2%,4.0°)(82.8%,5.5°)

mixture or mono/multi-exponential decay. Here we choose both Gaussian mixture and non-Gaussian mixture to validate our methods. We set $S(\mathbf{q}) = \sum_{i=1}^{M} p_i f_i(\mathbf{q})$, $f(\mathbf{q}) = G(\mathbf{q})$ for a Gaussian mixture model and $f(\mathbf{q}) = 0.5G(\mathbf{q}) + 0.5T(\mathbf{q})$, $T(\mathbf{q}) = \exp(-\sqrt{2q^2 \mathbf{u}^T \mathbf{D}\mathbf{u}})$ for a non-Gaussian mixture model. It could be proved that the ODF of $T(\mathbf{q})$ are the same as the ODFs of $G(\mathbf{q})$, although they have different EAPs [9]. The EAP of $T(\mathbf{q})$ is $P(R\mathbf{r}) = \frac{16\pi}{\sqrt{|\mathbf{D}|}(4+4\pi^2 R^2 \mathbf{r}^T \mathbf{D}^{-1} \mathbf{r})^2}$. Thus we have the analytical ground truth of EAP. We use the same way in [2] to add Rician noise with $SNR = 1/\sigma$. SNR is defined as the ratio of maximal signal intensity of $S(0) = 1$ to the standard deviation σ of complex Gaussian noise. We reconstructed EAP profile $P(R_0 \mathbf{r})$ at $R_0 = 15\mu m$ from our method and DOT in different configurations of signal generators with different fiber numbers (1 or 2), eigenvalues of $\mathbf{D}$, SNR, angle between 2 fibers. See Table 1, where (2, [1.7,0.3,0.3]e-3, 35, 60) means two fibers ($M = 2$), eigenvalues are [1.7,0.3,0.3]e-3, angle is 60°. and so on. For each configuration, data in 4 shells (b=500,1000,2000,3000s/mm^2) were generated for 1000 trials. For DOT, 4 order SH with $\lambda = 0.006$ was chosen for single shell data. For SPFI, we use all data in 4 shells and chose $N = 1$ for $SNR = 10$, and $N = 2$ for others and $L = 4$, $\lambda_l = 1e - 8$ $\lambda_n = 1e - 8$, $\zeta = 700$ for all experiments. We recorded the percentage of correct number of detected maximum of estimated EAP profile and the mean of angular error. The experiments showed that SPFI works better in the configurations with low anisotropy, much noise and non-exponential decay. Please note that we did not compare our method with DOT in multi-exponential model [6], because it is impractical as discussed in the introduction part.

Phantom data. We applied SPFI to a public phantom data with 3 shells with b-values of 650,1500,2000s/mm^2 respectively. This data has been used in the fiber cup contest in MICCAI 2009 to evaluate tracking methods [12]. The anisotropy of this data is very low, which makes it hard to detect the fibers. We believe that it is complex enough to evaluate different reconstruction methods and tracking methods. We compare our reconstruction method using 3 shells with DOT using one shell (b=2000) using Laplacian regularization term $\lambda = 0.006$ [2]. For SPFI, we choose $L = 4$, $\lambda_l = 5e - 8$ in the spherical part and $N = 1$, $\lambda_n = 1e - 9$ in the radial part [8]. Two crossing areas with EAP profiles in $R_0 = 15\mu m$, $17\mu m$ were chosen for visualization using min-max normalization [1]. To perform a fair comparison, we also tune the Laplacian regularization term lambda to 0.002 and 0.02 for region B. The results were shown in Fig. 1. It shows that SPFI could work well in the data with low anisotropy and non-exponential decay, which agrees with the results for synthetic data. that the method using 3 shells is
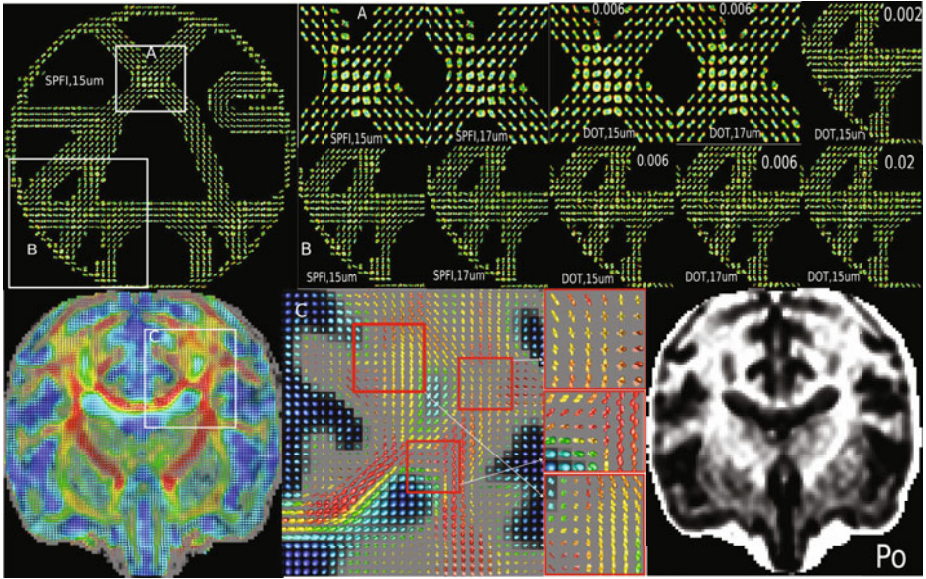
Fig. 1. First row: phantom data, from left to right: whole view of $P(R_0\mathbf{r})$, $R_0 = 15\mu m$ and $P(R_0\mathbf{r})$, $R_0 = 15\mu m, 17\mu m$ in region A and B of phantom data, calculated from SPFI and DOT. Region B was shown for DOT with $\lambda = 0.002, 0.006, 0.02$. Second row: real data result from SPFI, from left to right: whole view of $P(R_0\mathbf{r})$, $R_0 = 15\mu m$ and EAP in region C and *Po* of the real data

better. The bad performance of DOT is probably because of the modeling error of the mono-exponential assumption.

Real data. We tested our method using real monkey data with 3 shells (b=500, 1500, 3000), 30 directions at each b value, TE/TR/matrix=$120ms/6000ms/128 \times 128$. We set $L = 4$, $N = 2$, $\lambda_l = 5e - 9$, $\lambda_n = 1e - 9$ and show the results of $P(R_0\mathbf{r})$ at $R_0 = 15\mu m$. The glyphs were colored by GFA calculated from EAP profile [1]. Please note that we did not do any normalization here, e.g. min-max normalization [1]. That is because of two reasons. 1) the EAP profiles in white matter seem sharp enough and the profiles in CSF and gray matter are almost isotropic. 2) we will lost the radial information if we do some normalization. Please note that the radial information in EAP is also important compared with its peaks. It might be used to infer the axonal diameter and it is sensitive to white-matter anomalies [14]. From the results, we can see that the CSF has the largest probability (glyph size) compared with white matter and gray matter, just like the visualization of tensors in DTI. Tensors cannot illustrate and recover crossing fibers, while EAP profiles can. We also show in Fig. 1 the *Po* calculated from SPFI.

4   Conclusion

We proposed Spherical Polar Fourier Imaging (SPFI), a novel model-free fast robust analytical EAP profile reconstruction method based on Spherical Polar Fourier expression (SPFE) of the signal in **q**-space. It provides a linear analytical closed form to estimate

the EAP profile from the signal under SPFE. It is a linear transformation that is independent of data. This transformation matrix is just calculated only once for a whole data set, which makes SPFI extremely fast. SPFI can avoid the error from unrealistic assumptions and can naturally combine the signals with different b-values. The experimental results from synthetic data, phantom data and real data show that SPFI can perform better than DOT, especially for the data with low anisotropy, low SNR and non-exponential decay.

References

1. Tuch, D.S.: Q-ball imaging. Magnetic Resonance in Medicine 52, 1358–1372 (2004)
2. Descoteaux, M., Angelino, E., Fitzgibbons, S., Deriche, R.: Regularized, fast and robust analytical q-ball imaging. Magnetic Resonance in Medicine 58, 497–510 (2007)
3. Basser, P.J., Mattiello, J., LeBihan, D.: MR diffusion tensor spectroscropy and imaging. Biophysical Journal 66, 259–267 (1994)
4. Wedeen, V.J., Hagmann, P., Tseng, W.Y.I., Reese, T.G., Weisskoff, R.M.: Mapping complex tissue architecture with diffusion spectrum magnetic resonance imaging. Magnetic Resonance In Medicine 54, 1377–1386 (2005)
5. Wu, Y.C., Alexander, A.L.: Hybrid diffusion imaging. NeuroImage 36, 617–629 (2007)
6. Özarslan, E., Shepherd, T.M., Vemuri, B.C., Blackband, S.J., Mareci, T.H.: Resolution of complex tissue microarchitecture using the diffusion orientation transform (DOT). NeuroImage 31, 1086–1103 (2006)
7. Descoteaux, M., Deriche, R., Bihan, D.L., Mangin, J.F., Poupon, C.: Diffusion propagator imaging: Using Laplace's equation and multiple shell acquisitions to reconstruct the diffusion propagator. In: Prince, J.L., Pham, D.L., Myers, K.J. (eds.) Information Processing in Medical Imaging. LNCS, vol. 5636, pp. 1–13. Springer, Heidelberg (2009)
8. Assemlal, H.E., Tschumperlé, D., Brun, L.: Efficient and robust computation of PDF features from diffusion MR signal. Medical Image Analysis 13, 715–729 (2009)
9. Gradshteyn, I., Ryzhik, I.: Table of Integrals, Series, and Products. Elsevier, Amsterdam (2007)
10. Tristán-Vega, A., Aja-Fernández, S.: DWI filtering using joint information for DTI and HARDI. Medical Image Analysis 14, 205–218 (2010)
11. Descoteaux, M., Wiest-Daessle, N., Prima, S., Barillot, C., Deriche, R.: Impact of Rician adapted non-local means filtering on HARDI. In: Metaxas, D., Axel, L., Fichtinger, G., Székely, G. (eds.) MICCAI 2008, Part II. LNCS, vol. 5242, pp. 122–130. Springer, Heidelberg (2008)
12. Poupon, C., Rieul, B., Kezele, I., Perrin, M., Poupon, F., Mangin, J.: New diffusion phantoms dedicated to the study and validation of high-angular-resolution diffusion imaging (HARDI) models. Magnetic Resonance In Medicine 60(6), 1276–1283 (2008)
13. Aganj, I., Lenglet, C., Sapiro, G., Yacoub, E., Ugurbil, K., Harel, N.: Reconstruction of the orientation distribution function in single and multiple shell q-ball imaging within constant solid angle. Magnetic Resonance in Medicine (2009)
14. Cohen, Y., Assaf, Y.: High b-value q-space analyzed diffusion-weighted MRS and MRI in neuronal tissues: A technical review. NMR in biomedicine 15, 516–542 (2002)